

- A. A. Akhundov, D. Yu. Bardin, and N. M. Shumeiko, *Sov. J. Nucl. Phys.* **26**, 660 (1977).
20. C. D. Jeffries, *History of the Development of Polarized Targets* in Proc. Ninth Int. High-Energy Spin Physics Symposium, Bonn, FRG, K. H. Altoff and W. Meyer, eds. (Springer-Verlag, Berlin, 1990); W. Meyer, *Present Status of Polarized Solid Targets*, Proc. Eleventh Int. High Energy Spin Physics Symposium, Bloomington, Indiana, K. Heller and S. Smith, eds. (AIP Press, New York, 1994); B. Adeva et al., *Nucl. Instrum. Methods* **A349**, 334 (1994), available as CERN preprint CERN-PPE-94-54 (1994)
 21. G. D. Cates et al., *Nucl. Instrum. Methods* **A356**, 148 (1995).
 22. SLAC E143, K. Abe et al., SLAC-PUB-95-6734 (1994); and K. Abe et al., *Phys. Rev. Lett.* **75**, 25 (1995).
 23. B. Adeva et al., *Phys. Lett.* **B302**, 533 (1993).
 24. SLAC E143, K. Abe et al., SLAC-PUB-95-6982 (1995).
 25. R. L. Jaffe and X. Ji, *Phys. Rev.* **D43**, 724 (1991); E. V. Shuryak and A. I. Vainshtein, *Nucl. Phys.* **B201**, 141 (1982); L. Mankiewicz and Z. Rysak, *Phys. Rev.* **D43**, 733 (1992); X. Artu and M. Mekfi, *Z. Phys.* **C45**, 699 (1990); J. L. Cortes, B. Pire, and J. P. Ralston, *Z. Phys.* **C55**, 409 (1992).
 26. H. Burkhardt and W. N. Cottingham, *Annals of Physics* **56**, 453 (1970).
 27. S. Wandzura and F. Wilczek, *Phys. Lett.* **B72**, 195 (1977).
 28. J. L. Cortes et al., *Z. Phys.* **C55**, 409 (1992).
 29. X. Song and J. S. McCarthy, *Phys. Rev.* **D49**, 3169 (1994), **D50**, 4718 (1994) (Erratum); X. Song, INPP-UVA-95/04 (1995); and private communications for values at $Q^2 = 5 \text{ (GeV/c)}^2$.
 30. M. Stratmann, *Z. Phys.* **C60**, 763 (1993), and private communication for values at $Q^2 = 5 \text{ (GeV/c)}^2$.
 31. SLAC E143, K. Abe et al., SLAC-PUB-95-6997 (1995).

12 References

1. J. Ashman et al., Phys. Lett. **B206**, 364 (1988).
2. J. Alguard et al., Nucl. Instrum. Methods **163**, 29 (1979).
3. W. B. Atwood et al., Phys. Rev. **D18**, 2223 (1978).
4. E. L. Garwin et al., Helv. Phys. Acta **47**, 393 (1974); and D. T. Pierce and F. Meier, Phys. Rev. **B13**, 5484 (1976).
5. R. Alley et al., SLAC-PUB-95-6489, Nucl. Instrum. Methods **A365**, 1 (1995).
6. P. Zorabedian, Ph.D. thesis, Stanford University; available as SLAC Report 248 (1982).
7. T. Maruyama et al., Phys. Rev. Lett. **66**, 2351 (1991), T. Nakanishi et al., Nagoya University Preprint DPNU-91-23, (1991); and T. Maruyama et al., Phys. Rev. **B46**, 4261 (1992).
8. For example, see A. Y. Chao and J. R. Arthur, Progress in Solid-State Chemistry **10**, 157 (1975).
9. Paul Horowitz and Winfield Hill, *The Art of Electronics* (Cambridge University Press, 1989) pp. 437-446.
10. T. J. Gay and F. B. Dunning, Rev. Sci. Instrum. **63**, 1635 (1992).
11. G. Mulhollan (SLAC), private communication
12. L. G. Levchuk, Nucl. Instrum. Methods **A345**, 496 (1994).
13. M. Swartz et al., Nucl. Instrum. Methods **A363**, 526 (1995).
14. B. W. Montague, Physics Reports **113** No. 1, (1984); also V. Bargmann, L. Michel, and V. L. Telegdi, Phys. Rev. Lett. **2**, 435 (1959).
15. L. W. Whitlow et al., Phys. Lett. **B282**, 475 (1992), and L. W. Whitlow et al., Phys. Lett. **B250**, 193 (1990).
16. T. V. Kuchto and N. M. Shumeiko, Nucl. Phys. **B219**, 412 (1983).
17. I. V. Akusevich and N. M. Shumeiko, J. Phys. **G20**, 513 (1994).
18. SLAC E143, K. Abe et al., SLAC-PUB-6508 (1994); and Phys. Rev. Lett. **74**, 346 (1995).
19. L. W. Mo and Y. S. Tsai, Rev. Mod. Phys. **41**, 205 (1969); also Y. S. Tsai, SLAC-PUB-848 (1971); see also A. A. Akhundov, D. Yu. Bardin, and W. Lohmann, JINR E2-86-204 (1986); A. A. Akhundov, D. Yu. Bardin, and N. M. Shumeiko, Sov. J. Nucl. Phys. **44**, 1212 (1986); D. Yu. Bardin and N. M. Shumeiko, Sov. J. Nucl. Phys. **29**, 499 (1979); and

End Station A, with its 50 GeV Upgrade beam, is available for future experiments that can satisfy the SLAC Program Advisory Committee's tough criteria. Those are, of course, that the physics objectives be of high quality, and the cost to the SLAC program be modest, at least until the B-Factory project is completed. At present, no proposals have passed this tough test, so there are no scheduled experiments beyond E155. The facility is available for future proposals which effectively utilize its unique capabilities.

10 Experimental Results on the Q^2 Dependence in the Proton Data

These results have been presented in another talk at this school, and have been published. ³¹

11 The 50 GeV Upgrade

Since the advent of the SLC (the SLAC Linear Collider) project, the SLAC linac beams have been able to accelerate electrons up to energies in excess of 50 GeV. The spin-structure measurements benefit from higher-energy beams, both in the low- x reach (where a $Q^2 > 1$ (GeV/c)² cut is imposed) and in the high- x reach (where a $W > 2$ GeV cut is imposed). The 50 GeV Upgrade was proposed in 1990 as a modest project to extend the physics reach of the spin-structure experiments at SLAC.

The End Station A facility resides at the end of the linac, but to the left and off the machine axis. Beams from the linac are transported through a series of bending magnets and quadrupoles to reach the End Station A targets. The original beamline operated up to 32 GeV. By adding additional dipole magnets, the energy can be raised to 50 GeV. The proposal consisted in adding four dipole magnets to the original set of eight, and reducing the magnet gaps by one-half to save power. The resulting beamline has now been installed, and the power consumption at 50 GeV is below the old value operating at 25 GeV. The focusing elements did not require modification.

The 50 GeV Upgrade was approved in 1992 and two experiments, E154 (which extends the ³He measurements of E142) and E155 (which extends the NH₃ and ND₃ measurements of E143) were approved for running at 50 GeV. Both experiments will provide high-statistics data for x -values down to 0.018 and $\langle Q^2 \rangle \approx 5$ (GeV/c)². The E154 experiment is scheduled to commence data taking in October 1995 and to end in December 1995. The E155 experiment is presently expected to run in late 1996.

The 50 GeV experiments are now underway and will be completed in late 1996. The 50 GeV data will expand the Q^2 - and x -range of the data from SLAC, and errors resulting from these data will reduce the uncertainties on the Bjorken and Ellis-Jaffe sum rules by a factor of 2 relative to the earlier experiments, E142 and E143.

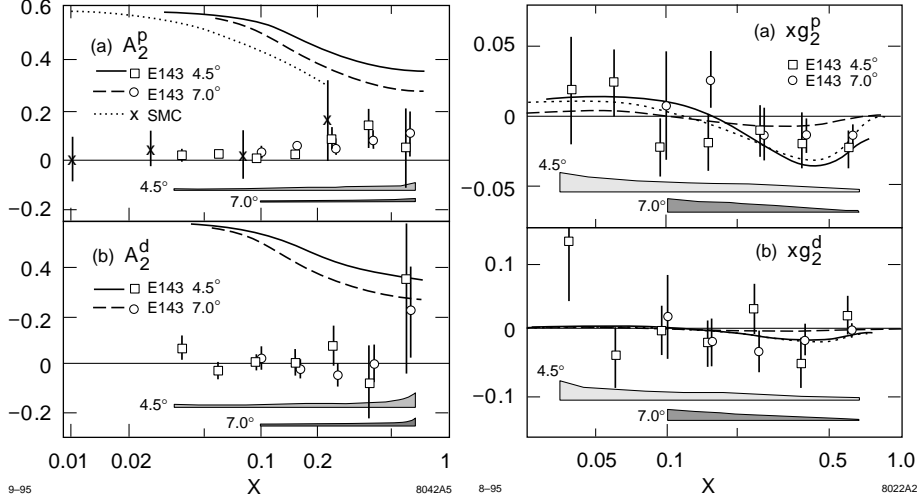


Figure 22: (i) The transverse asymmetries $A_2^p(x)$ from E143 experiment and the SMC data and $A_2^d(x)$ from E143 are shown. The curves show the positivity limits for the data indicated. (ii) The spin-dependent structure functions $xg_2^p(x)$ and $xg_2^d(x)$ from E143 are shown. The solid line represents g_2^{WW} from fits to g_1 , and the dashed and dot-dashed curves are two models for g_2 described in references 29 and 30. Systematic errors are indicated by the shaded areas.

where m and M are quark and nucleon masses, $h_T(x, Q^2)$ is a leading-twist term related to quark polarization in a transversely polarized nucleon, and ξ is a higher-twist term related to quark-gluon interactions. Thus the structure function g_2 is generally regarded to be a good place to look for higher-twist effects in deep-inelastic scattering.

Figure 22a shows the E143 results for A_2^p and A_2^d . There is a constraint, known as the positivity limit, which gives $|A_2| \leq \sqrt{R(x, Q^2)}$. The positivity limits for A_2 are also shown in Figure 22a.

Figure 22b shows $xg_2^p(x)$ and $xg_2^d(x)$ that result from the E143 data. Two bag models^{29,30} are also indicated, together with the leading-twist expectation, g_2^{WW} . Within the present accuracy of the data, the models are allowed, but the data do show that higher-twist terms are needed. A pure leading-twist term is an equally good fit to the data.

Experimentally, g_2 is measured by rotating the target polarization to a transverse orientation. In this configuration, an asymmetry is measured

$$A_{\perp} = \frac{\sigma_+ - \sigma_-}{\sigma_+ + \sigma_-} = \frac{N_+ - N_-}{N_+ + N_-} \frac{C_N}{fP_bP_t} + A_{\text{rad}} ,$$

where σ_+ , σ_- , N_+ , and N_- are the cross section and counts for + and - beam helicity for transverse target spin.

The factors C_N , f , P_b , and P_t correct for the nitrogen nucleus polarization, the fraction of unpolarized nucleons in the target, the beam polarization, and the target polarization, respectively. A_{rad} is the electromagnetic radiative corrections, computed by formulae and models of the data, as outlined in Section 5.

Using both the A_{\parallel} and the A_{\perp} asymmetries, then

$$g_2(x, Q^2) = \frac{yF_1(x, Q^2)}{2D} \left[\frac{E + E' \cos \theta}{E' \sin \theta} A_{\perp} - A_{\parallel} \right]$$

and

$$A_2(x, Q^2) = \frac{\gamma(2-y)}{2D} \left[A_{\parallel} + \frac{y(1+xM/E)}{(1-y)\sin\theta} A_{\perp} \right] ,$$

where $\gamma = 2Mx/\sqrt{Q^2}$.

There is a sum rule for g_2 , the Burkhardt-Cottingham sum rule:²⁶

$$\lim_{Q^2 \rightarrow \infty} \int_0^1 g_2(x, Q^2) dx = 0.$$

and the Wandzura-Wilczek relation:²⁷

$$g_2^{WW}(x, Q^2) = -g_1(x, Q^2) + \int_x^1 g_1(x', Q^2) dx' ,$$

which gives the connection between g_1 and g_2 . The quantity g_2^{WW} is a leading twist component of g_2 . Often defined is an additional piece for g_2 :

$$g_2 = g_2^{WW} + \bar{g}_2.$$

The term \bar{g}_2 contains higher-twist parts. In the presence of higher twist, a suggested form is²⁸

$$g_2(x, Q^2) = g_2^{WW}(x, Q^2) - \int_x^1 \frac{\partial}{\partial y} \left(\frac{m}{M} h_T(y, Q^2) + \xi(y, Q^2) \right) \frac{dy}{y}.$$

at $Q^2 = 3 \text{ (GeV/c)}^2$. The experimental data are summarized by two ellipses which give the 1σ and 2σ boundaries. The Bjorken sum rule passes through the 1σ contour, demonstrating that this sum rule is satisfied with combined experimental errors of $\pm 7\%$. The Ellis-Jaffe sum rules are violated by approximately 7σ . This failure of the Ellis-Jaffe sum rules has been known since the EMC results were published. This failure became publicized as the “spin crisis”, and the strange quarks in the quark sea have been implicated in this failure.

The Ellis-Jaffe sum rules are based on model assumptions regarding the spin of the quarks in the nucleon. Specifically, Ellis-Jaffe assumed that the strange quarks were unpolarized ($\Delta s = s^\uparrow - s^\downarrow + \bar{s}^\uparrow - \bar{s}^\downarrow = 0$). The present understanding is that $\Delta s \approx -0.1$ to -0.2 . The net strange-quark spin is opposite to that of the nucleon. How this arises within a nucleon is not understood.

Future experiments may help elucidate these matters. First, experiments are needed at higher energies to study the $x \rightarrow 0$ limit in the structure functions. Until it is shown *experimentally* that the structure functions behave in a smooth fashion near $x = 0$, there will always remain uncertainties in the value of the integrals I_p , I_n , and I_d . Second, experiments which are sensitive to the gluon spin structure, ΔG , must be performed. This is difficult in deep inelastic scattering, since electrons or muons do not couple directly to the gluons. In deep inelastic scattering, the gluon contributions can only be inferred by the evolution of the structure functions, a difficult technique at best, considering the present precision and kinematic range of the data. Polarized proton beams at RHIC have recently been proposed. Experiments using these polarized beams could measure ΔG .

9 The g_2 Structure Function

The E143 experiment has recently reported measurements on the second structure function $g_2(x)$.²⁴ The g_2 structure function is well established formally, and readily measured experimentally. It has been poorly understood, especially in early literature on this subject. It has been difficult to discuss informally, because it lacks simple interpretation in the quark-parton model. Recent work has gone a long way toward clarifying the role of g_2 and its meaning in deep inelastic scattering.²⁵

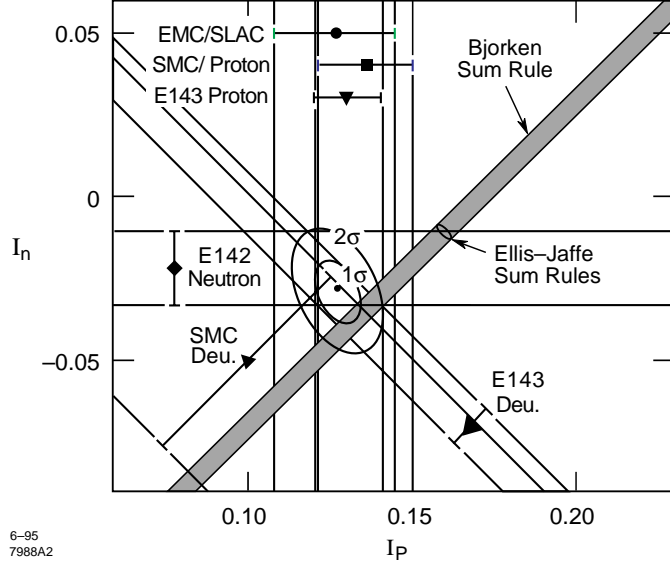


Figure 21: The experimental sum rules for the proton, deuteron, and neutron are shown in two dimensions. The one- and two-sigma contours in the $I_n - I_p$ plane are given, with the predictions of the Bjorken sum rule and the Ellis-Jaffe sum rules.

once per day. Polarization of the targets thus would vary during data taking, and monitoring of the polarization signal by an NMR technique allowed for accurate values of polarization to be recorded.

The results of the deuterium runs at 29.13 GeV are shown in Figure 19,²² along with SMC deuterium data.²³ Figure 20 shows $xg_1^d(x)$ for the E143 data and compares the derived values for $xg_1^n(x)$ from the E142 experiment. The results for E143 agree well with the earlier E142 data. The E142 data were at a $\langle Q^2 \rangle$ value of 2 (GeV/c)², while for E143, $\langle Q^2 \rangle = 3$ (GeV/c)².

Figure 21 summarizes the present status of the proton, neutron, and deuterium integrals. In this plot, I_n and I_p are the axes, and the data for the proton integral I_p from three experiments, I_n from E142, and I_d from E143 and SMC each establish a band in this plane. The Bjorken sum rule, $I_p - I_n = 0.171 \pm 0.008$ (at $Q^2 = 3$ (GeV/c)²) is a diagonal band with its width arising from the uncertainty in α_s (assumed to be 0.35 ± 0.05). The Ellis-Jaffe sum rules define a point in the plane, $I_p = 0.160 \pm 0.007$ and $I_n = -0.011 \pm 0.004$

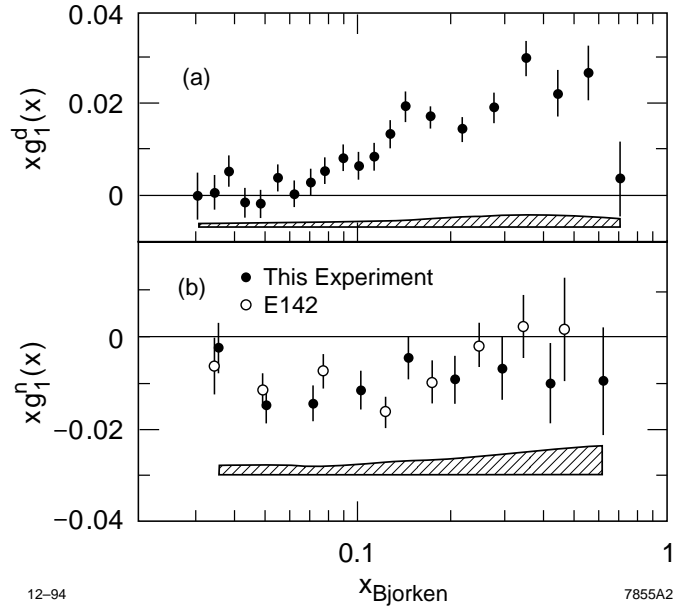


Figure 20: The spin-structure function $xg_1^d(x)$ from E143 (1994) and the comparison of the structure functions $xg_1^n(x)$ from E142 and E143.

8 The Deuterium and Helium-3 Data

The E143 experiment utilized an ammonia target for polarization of the free protons in NH_3 . By the substitution of deuterium for the hydrogen in the ammonia molecule, the deuterium can be polarized using similar techniques to polarizing of the proton target. The E143 target cells were developed by the University of Virginia group to allow both NH_3 and ND_3 cells to reside in the target cryostat together. By a simple vertical adjustment, the NH_3 or ND_3 cell could be swapped into the beam position. The strategy employed during E143 was to expose NH_3 to the beam until degradation of polarization set in, due to radiation damage. The ND_3 target would be inserted and exposed for a period of time until its polarization was degraded. The radiation-induced damage could be “annealed” away by raising the temperature to approximately 80° Kelvin. Following an anneal cycle, polarization would recover and data taking would resume. Annealing of the targets was required approximately

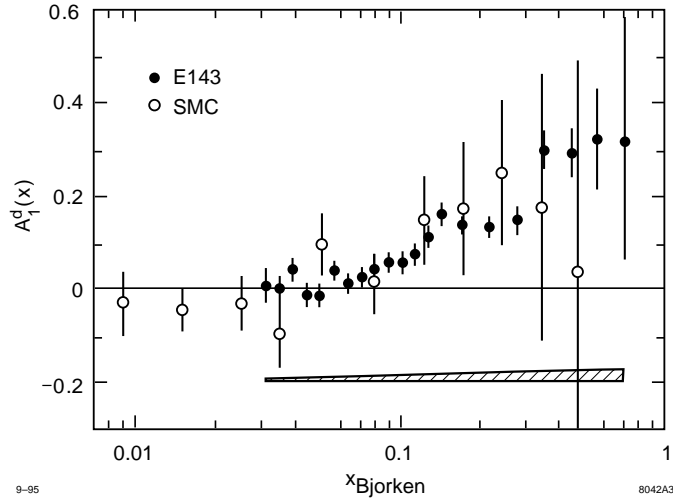


Figure 19: The physics asymmetry for the deuteron, $A_1^d(x)$, from E143 (1994) and SMC (1993).

A polarized ^3He target operates on an entirely different set of principles.²¹ The E142 target consisted of a 30-cm-long glass cell filled with 10 atmospheres of ^3He gas at room temperature. The target structure consisted of two connected glass cells, one for the electron beam, and one for the pumping laser beam. The pumping cell holds a rubidium vapor, mixed in with the ^3He ; the rubidium concentration is adjusted by the temperature of the cell, which controls the rubidium vapor pressure. Circularly polarized light (σ^+) at $\lambda = 795$ nm pumps the electronic ground state, $5^2S_{1/2}$, to a higher level, $5^2P_{1/2}$ ($m_z = -1/2$ to $m_z = +1/2$). With sufficiently high power, one of the spin substates in the rubidium ground state ($m_z = -1/2$ or $m_z = +1/2$) can be fully depleted, leaving a polarized vapor of atomic rubidium. Subsequent collisions with the ^3He atoms transfers the rubidium electronic spin (with low probability) to the ^3He nucleus. Continual pumping with the laser leads to a buildup of the ^3He nucleus polarization through this process. Migration of the ^3He atoms to the lower cell results in net target polarization. The E142 target cells achieved polarizations of 35 – 40%. The polarization was monitored by an NMR technique.

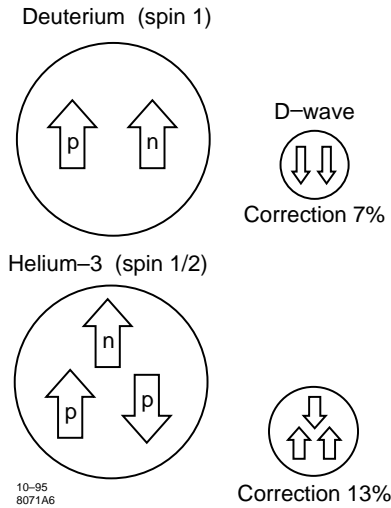


Figure 18: The deuterium and ^3He nuclei serve as sources of polarized neutrons.

defined, resulting in the deuterium nucleus being polarized. The degree of polarization in the target depends on the power level of the microwave and on the time constants for relaxation back to the ground state.

Pre-irradiation of the target material is required to generate the polarization. Radiation introduces broken electronic bonds, and the unpaired bonds are involved in the process of polarization. Once the target is used in a beam of electrons, the material undergoes further radiation damage. Maximizing the target polarization requires optimizing the various parameters, including the amount of pre-irradiation, the temperature at which the target undergoes pre-irradiation, beam current during the experimental running, and other factors. Once radiation damage has become too severe, the polarization is seen to decrease. Warming the target to higher temperatures “anneals” the material, recovering somewhat the effects due to radiation damage. The time between annealing cycles was typically 24 hours during the E143 running.

For E143, the deuterium target polarization varied between 25% and 40%. Monitoring of the time-varying polarization by an NMR technique provided the time-dependent values that were needed in the physics analysis. The overall target polarization uncertainty for the ND_3 running was $\pm 5\%$.

Table 2: Sources of Systematic Errors—E143 at 29.1 GeV

Parameter	Target	Value	Contribution to $\Delta \int_0^1 g_1 dx$ (%)
P_b		0.84	3
P_t	p	55-80%	2.5
P_t	d	25%	5
f	p	0.13-0.17	2.4
f	d	0.22-0.25	5
C_N	p	0.98	0.5
C_N	d	1.016	0.5
A_{rad}	p	.002-.005	2.5
A_{rad}	d	.002-.005	5
D'		x-dependent	3
F_1		x-dependent	2.5
extrapolation errors:			
$\int_0^{x_{\text{min}}} g_1^p dx$	p	0.008	4
$\int_{x_{\text{max}}}^1 g_1^p dx$	p	0.001	1
$\int_0^{x_{\text{min}}} g_1^d dx$	d	0.001	2.5
$\int_{x_{\text{max}}}^1 g_1^d dx$	d	0.000	2.5
Total	p		7
Total	d		10

Deuterium targets have been discussed fully elsewhere.²⁰ The deuterium target is polarized by the technique known as dynamic nuclear polarization, or DNP. A target of $^{15}\text{ND}_3$ material (in the shape of a cylinder of approximately 3 cm length by 2 cm diameter) is placed in a 5 Tesla magnetic field at 1° Kelvin. The temperature is held at this level by a liquid ^4He bath and an evaporation refrigerator. The 5 Tesla magnetic field is generated using a superconducting solenoid whose coils are arranged in a Helmholtz geometry. The high magnetic field splits the energy levels of the deuterium nucleus-electron configuration into well defined spin states. The input of microwave energy of a well defined frequency (140 GHz) induces transitions from the ground state to an upper state. The deuteron spin projection associated with the upper state is well

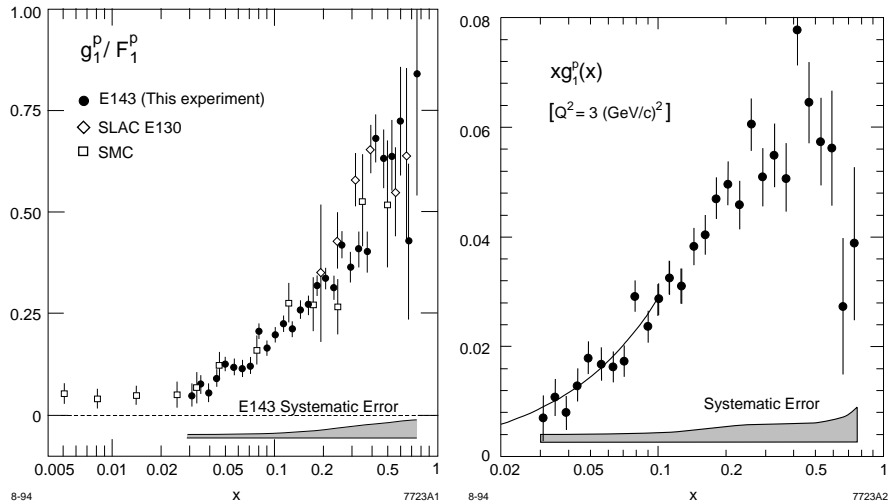


Figure 17: The ratios g_1^p/F_1^p from E130, E143, and SMC, and xg_1^p from E143 as a function of x . The errors are statistical only. The systematic errors are indicated by the shaded region. The solid line on the xg_1^p plot is the curve E143 used to extrapolate to $x=0$.

subtracted. Errors from the proton measurement propagate into the resulting value for the neutron integral. By using the deuterium target as a source of neutrons, the neutron integral can never be better than the corresponding measurements for the proton integral.

The ^3He nucleus can be a better source of polarized neutrons. The ^3He has two protons plus a neutron as constituent nucleons. The two proton spins are oppositely aligned, approximately cancelling their net spin contribution. The neutron has its spin aligned mostly in the ^3He spin direction. There exists a small probability of finding the protons with both spins aligned and the neutron with its spin opposite to that of the helium nucleus. Corrections for the second configuration are estimated to be about 13%, going from the helium structure functions to the neutron structure functions. However, the neutron is basically scaled from the ^3He measurements, except for these small corrections. The ^3He thus has the advantage that it does not require a proton subtraction and this results in correspondingly less errors. In practice, the ^3He target gives a neutron error with about one-half the errors of the deuterium target, other experimental factors being similar.

cases, models of σ and $\Delta\sigma = \sigma^{\uparrow\uparrow} - \sigma^{\uparrow\downarrow}$ are needed. Where data exist, the global fits are used. In some regions of the kinematic plane, the data are lacking at the present time, so reasonable assumptions are made and reasonable errors for those assumptions are assigned.

Corrections are made to the *experimental* asymmetries, A_{\parallel} and A_{\perp} . These corrections turn out to be small because A_{\parallel} and A_{\perp} are relatively constant over the broad regions that affect them. Figures 16a and b show the experimental asymmetries A_{\parallel}^p and A_{\perp}^p versus x for the beam energy of 29.13 GeV, and the corrections as calculated and applied. The deuteron data are similar, but not shown here.

6 The Proton Measurements

Having applied the radiative correction factors discussed in the previous section, one can turn to more mundane, but equally important, factors. Table II lists the typical values for the correction factors C_N , f , P_b , and P_t for the E143 data at 29.13 GeV.¹⁸ Figure 17a shows the proton data, with g_1/F_1 plotted against x on a logarithmic scale. Systematic errors for the E143 experiment are indicated by the shaded regions. Figure 17b also shows the E143 proton data as $xg_1(x)$ versus x . The solid line shows the fit $g_1 = \text{constant}$ for values at low x . This fit is used to extrapolate to $x = 0$ below the measured data. E143 evaluates the integral $I_p = \int_0^1 g_1^p(x) dx = 0.129 \pm 0.004 \pm 0.009$ at $Q^2 = 3 \text{ (GeV}/c)^2$.

7 Neutron Targets

Figure 18 illustrates the differences between the deuteron and ^3He targets as a source of polarized neutrons. The deuterium nucleus is a spin-1 object with the constituent nucleons in a S-wave having spins aligned parallel to the deuterium spin. There is a small probability that the nucleons reside in a D-wave configuration, in which case the nucleon spins are antiparallel to the overall spin-1 axis of the nucleus. Corrections for the D-wave configuration lead to an overall 7% adjustment to the measured asymmetries (ie., to go from the deuterium integral I_d to the sum of the proton and neutron, $I_p + I_n$). To obtain the neutron integral from the deuterium integral, the proton integral must be

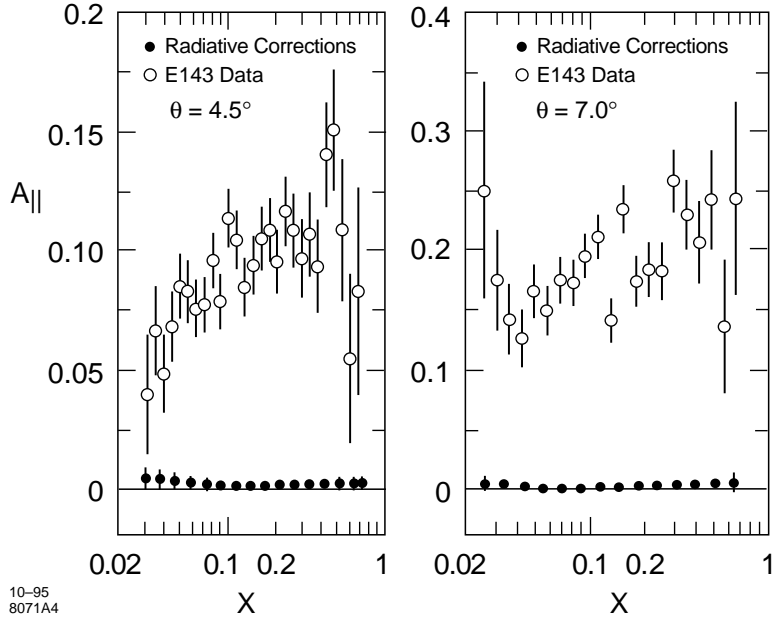


Figure 16: Experimental asymmetries for the proton from two E143 spectrometers at a beam energy of 29.13 GeV; (a) A_{\parallel} versus x ; (b) A_{\perp} versus x . The size of the contributions calculated for radiative processes is also indicated.

tions are indeed rather small.

An approach to radiative corrections has been developed over years of electron scattering experiments. This approach utilizes experimental results in which global fits to $F_2(x, Q^2)$ and $R(x, Q^2) = \sigma_L/\sigma_T$ have evolved.¹⁵ These global fits have become rather precise, so they are quite adequate for the calculations of the radiative effects.

Radiative corrections are artificially divided into “internal corrections”, corresponding to radiation for the internal lines in a Born diagram, and “external corrections”, where the electrons radiate photons at some distance away, due to the thick target effects (material before and after scattering). For the “internal” corrections, E143 used the work of Kuchto and Schumeiko¹⁶ and Akusevich and Schumeiko¹⁷ to generate the calculated corrections. For the “external” corrections, the work of Mo and Tsa¹⁹ (revised) is used. In both

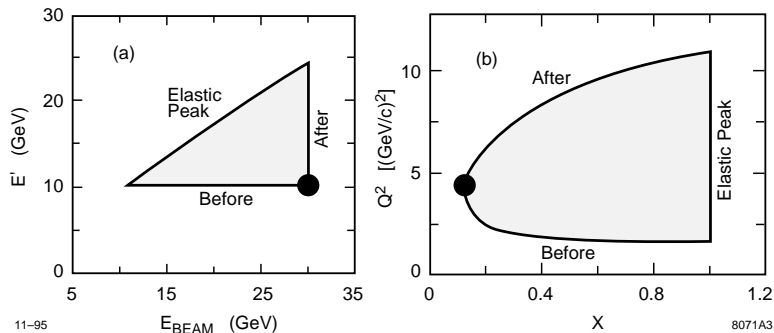


Figure 15: (a) A kinematic plane with E' versus E_{beam} ; events radiate from the “triangle” into the spectrometer setting denoted by the \bullet . (b) The same as in (a) but for the Q^2 versus x plane. “Before” and “After” refer to radiation of a photon before or after scattering.

flip probabilities are small, so they can be neglected in all cases except for the most precise work.

A closely related process is due to thick-target effects illustrated in Figure 14c. These processes are treated also in the radiative corrections. Figure 15a shows a kinematic diagram in the E' versus E_{beam} plane. A spectrometer defines a point in this plane (actually a small region defined by ΔE and $\Delta E'$) into which counts fall. In the presence of radiative processes, counts fall into this acceptance from distant points on the plane. Examples include elastic scattering, followed by radiation of a photon after the scattering, which reduces the value of E' so that it drops into the spectrometer acceptance. Radiation of a photon before it scatters reduces the incident energy of the scattering. Processes can also occur in which both the incident and outgoing electrons lose energy. Events from the interior of the triangle require energy loss both before and after the scattering.

In an $x - Q^2$ plane, these lines are distorted, as shown in Figure 15b.

Consider the asymmetry measurements; the radiation process carries into the spectrometer counts with varying asymmetries, depending on where they come from. Corrections to asymmetries can be quite different in scale than the corrections to cross sections. In an ideal situation, if the asymmetries were everywhere constant, then the correction to the measured asymmetry will be zero. In practice, asymmetries are not widely varying, so the radiative correc-

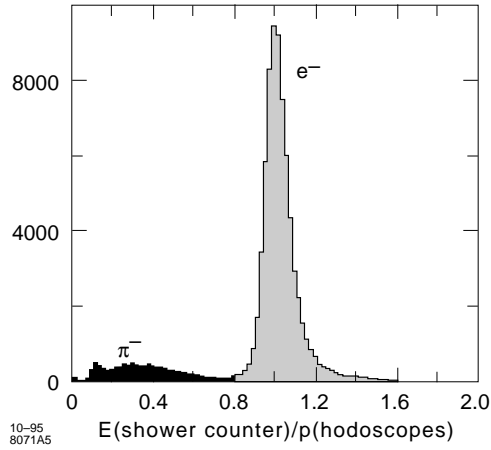


Figure 13: A typical spectra of $E(\text{shower counter})/p(\text{hodoscopes})$ for the 7° spectrometer. The peak at 1.0 corresponds to the electrons, while π^- events contribute a small background seen at $E/p < 1.0$.

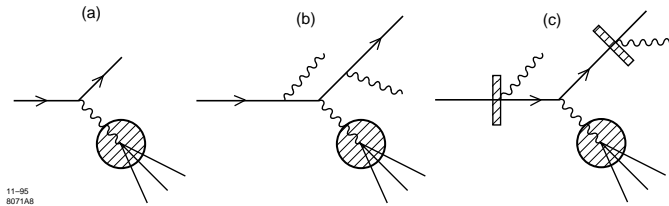


Figure 14: The electron scattering process, showing the bare process (a), the real process (b), and a third process involving thick targets (c).

is in Figure 14b. The radiation of soft or hard photons from the electron lines carry away energy and momentum. In so doing, they distort the kinematics interpretation (x, Q^2) of the event. The spectrometers have a resulting response in the (x, Q^2) plane that reaches to large parts of the plane. The purpose of the radiative corrections is to unfold this response and deduce the cross sections at the specific (x, Q^2) point. Since asymmetries are measured in the spin-dependent inelastic scattering process, the asymmetries associated with the radiated events which fall into the acceptance need to be unfolded. Doing this unfolding requires knowledge of the asymmetry from the whole kinematic plane.

The spin of the electrons can also flip in the scattering process. The spin-

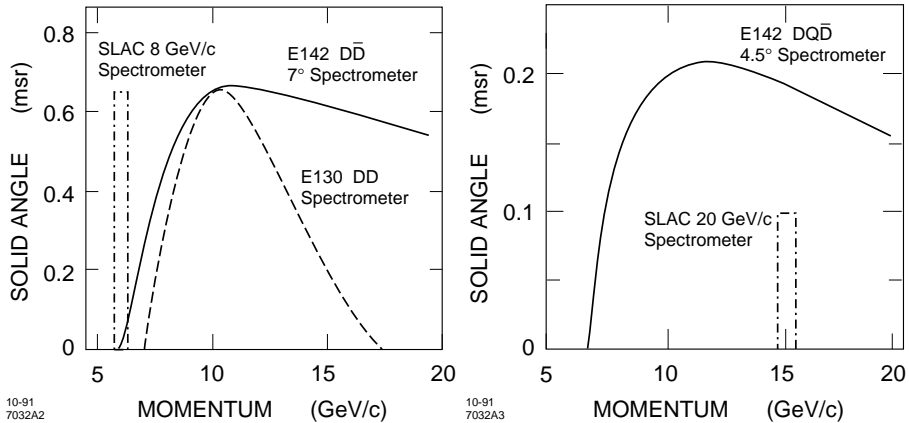


Figure 12: (a) The comparison is shown of the solid angle acceptances versus momentum for the 8 GeV/c spectrometer, the E130 DD spectrometer, and the E142/E143 D D-bar 7° spectrometer. (b) The comparison of the solid angle acceptances versus momentum for the 20 GeV/c spectrometer and the E142/E143 D Q D-bar 4.5° spectrometer.

hadronic showers from the π^- s generally fall below 1.0. The dark shaded area indicates those tracks that have been identified by a neural network algorithm as non-electromagnetic in origin.

The procedure for subtracting π^- s and those e^- s that come from *charge symmetric processes* is the following: the spectrometer is set to opposite polarity, so that π^+ s and e^+ s are detected. A short run on these positives is sufficient to measure the associated asymmetries (usually close to 0) and the rates. Subtraction of this signal from the total negative signal then corrects for e^- s and π^- s from all charge symmetric processes. The subtractions are small, typically $\leq 1\%$.

5 Radiative Corrections

Before discussing the data, it is perhaps valuable to revisit an old subject, radiative corrections. Traditionally, radiative corrections have been applied to unpolarized scattering. For spin-dependent structure functions, the process must be extended to the spin-dependent cross sections. The physics process under discussion is shown in Figure 14a, while the actual process being measured

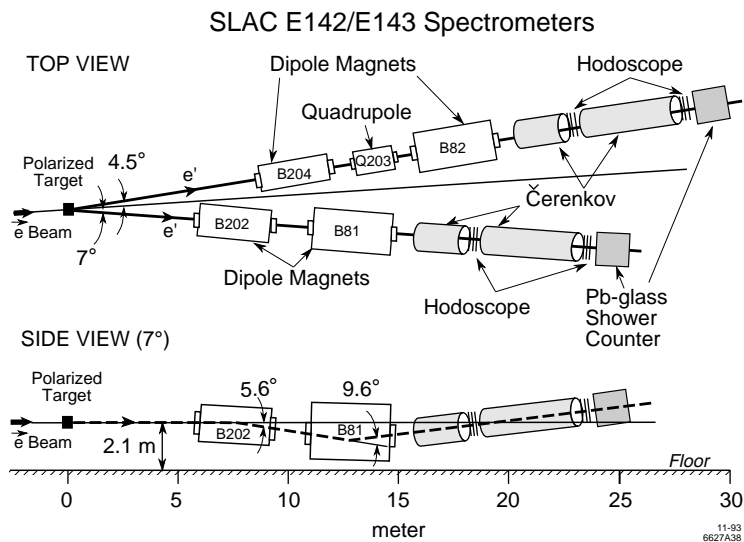


Figure 11: The layout of the E142/E143 spectrometers on the End Station A floor is shown. Two spectrometers operated in parallel, one at 4.5° and one at 7.0° .

The side view shows the reverse bends (denoted $D\bar{D}$) in the two spectrometers. The reverse-bend geometry has additional important benefits in that the magnets are located close the End Station A floor. Concrete shielding blocks, which are used to surround and cover the magnets, are themselves located close to the floor, a considerable help in the shielding design in earthquake-prone California. Figures 12a and 12b show the comparison of solid angle acceptances for various spectrometers used at SLAC. The broad range in momentum acceptance in the E142/E143 spectrometers allow a full x -range to be covered in one setting of the two spectrometers.

The spectrometers were instrumented with gas Čerenkov counters (pressured at $\approx 1/3$ atmosphere with nitrogen) and scintillator hodoscope arrays to give tracking information and π^- rejection for momenta below ≈ 11 GeV/ c . Figure 13 shows the electron and π^- signals that E143 saw in the 7° spectrometer. In this figure, the ratio $E(\text{from the shower counter})/p(\text{from hodoscope tracking})$ is binned for all triggers. The calibration procedure for the shower counter has adjusted the shower counter peak height to fall near 1.0. The

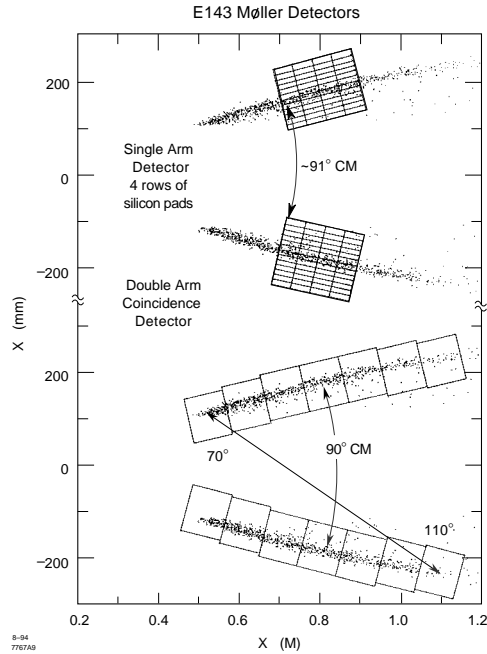


Figure 10: The Monte Carlo hits are shown at the face of the E143 Møller detectors. Silicon pad arrays detect the single hits, while the lead-glass shower counters operated in coincidence, one hit on the top, one on the bottom. The two systems are shown separated for clarity, but actually were overlapping.

4 Spectrometers

The spectrometers in the End Station A facility have evolved over a period of 25 years. The early set of spectrometers consisted of three, the 1.6 GeV/c, the 8 GeV/c, and the 20 GeV/c spectrometers. Each of these was free to rotate about a common point, the pivot, where the targets for the experiments resided. More recently, experiments have begun to use the magnets from these three spectrometers to construct specialized fixed-angle spectrometers on the End Station A floor. The newer designs allow for spectrometer optics that trade resolution (not needed in the deep inelastic regime) for increased solid angle acceptance (needed for higher statistics).

Figure 11 shows the layout of the E142/E143 spectrometers at 4.5° and 7° .

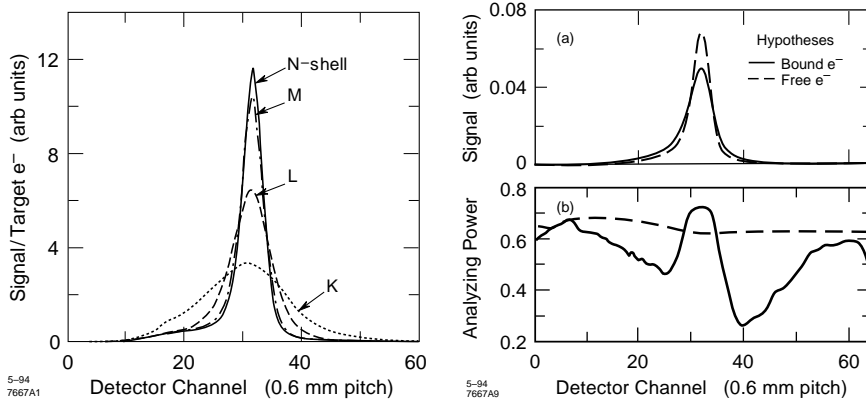


Figure 9: (i) A Monte Carlo prediction for the distribution of electrons in a SLAC Møller detector array for electrons that come from the K, L, M, or N shells in the Fe atom. (ii) A Monte Carlo prediction for the signal and associated asymmetry function for a SLAC Møller detector array, compared to what would be expected for free electrons.

unwanted backgrounds, provided that the counting rates in the detectors are not too high.

The SLAC experiment E143 used both single and double-arm techniques for polarimetry. Figure 10 illustrates the single-arm detectors (silicon pads) which overlay the double-arm coincidence detectors (lead glass). In the final analysis, the double-arm techniques proved to be more accurate, so the E143 analysis used the coincidence technique for its final data analysis.

Precession of the electron spin in the transport line has been well characterized in previous work.¹⁴ For the 24.5° bending angle of the transport line, the spin precesses ahead of the beam direction by $\theta_{\text{precess}} = [\pi E_{\text{beam}}/3.237 \text{ (GeV)}]$ radians. The choice of 29.13 GeV for the beam energy gives $\theta_{\text{precess}} = 9\pi$ corresponding to 4.5 full rotations of the spin relative to the beam direction. E143 used this spin precession to check the energy calibration of the transport line and energy slits, which proved to be accurate to ± 50 MeV.

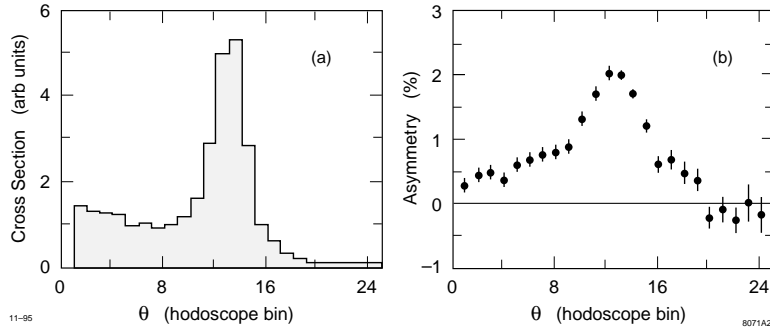


Figure 8: The Møller peak in a simple wire detector array shows the kinematic peak for elastic e-e scattering, sitting on a background from inelastic e-Fe scattering. The asymmetry associated with the elastic signal is proportional to the beam polarization P_e . The asymmetry in the channels to the left of the peak results from radiative tails of the e-e scattering mixed in with the e-Fe scattering.

carried by a bound electron can be ignored at these high energies, the longitudinal momentum must be considered. This component smears out the precise kinematics of a free electron in a way that must be accounted for.

Figure 9i shows the contributions to the Møller peak for the four shells, and Figure 9ii shows the resulting distortions to the asymmetry. The atomic binding effects can be understood in detail only with a detailed Monte Carlo calculation that accurately simulates the polarimeter geometry and materials. There is no universal correction that can be applied to single-arm Møller polarimetry to correct for the atomic binding effects.

An approach to curing the atomic binding problems of the single-arm Møller polarimetry lies in the coincidence measurement, or double-arm Møller polarimeter. In requiring a coincidence with both final state electrons, the background process from e-Fe scattering is eliminated. The Møller process is detected as a coincidence between two detectors on opposite sides of the beamline, appropriately placed as determined by the two-body kinematics. The detector acceptances can be rather broad to cover fully the smearing that occurs for deeply bound electrons. The bound electrons can be detected with full efficiency without the kinematic distortions being a problem. The resulting coincidence signal carries the same asymmetry as if the electrons were all free. The value of the coincidence technique lies in the fact it is essentially free of

small lab angle makes detection of the scattered electrons relatively simple in practice, because the detection systems are relatively small and compact.

Experimentally, an asymmetry is measured by:

$$A_{\text{Møller}} = \frac{\sigma^{\uparrow\uparrow} - \sigma^{\uparrow\downarrow}}{\sigma^{\uparrow\uparrow} + \sigma^{\uparrow\downarrow}} = 7/9 P_b^z P_t^z,$$

where $\sigma^{\uparrow\uparrow}(\sigma^{\uparrow\downarrow})$ is the cross section for longitudinal spins parallel (anti-parallel). Polarized target electrons are obtained by magnetizing an iron (Fe) foil and rotating the plane of the foil so that the polarized Fe electrons have a component along the beam direction. The Fe atom has 26 electrons, of which 2 are polarized. For a foil rotated so that the normal to the foil plane is at a tilt angle of 70° away from the beam axis

$$A_{\text{Møller}} = 7/9 \cdot 2/26 \cdot P_b^z \sin \theta_{\text{tilt}} \approx .058 P_b^z.$$

By analyzing the outgoing electrons in a simple spectrometer, scattered Møller electrons define kinematic line in a momentum-versus-angle plane beyond the exit of the magnet. This kinematic line can be detected in a wire chamber array placed behind a lead converter. Figure 8 shows an example of a Møller scattering signal and asymmetry, obtained in an experiment at SLAC. The peak of the asymmetry, in this example about 2%, scales with P_b^z , corresponding in this example to $\approx 40\%$ after backgrounds are subtracted. The background under the Møller peak comes from an irreducible source, namely the radiative Coulomb scattering of the electron from the Fe nucleus in the target.

Atomic binding of the electrons in the Fe atom distort the kinematics of the Møller scattering process. The atomic binding effects were first discussed by L. G. Levchuk,¹² and applied in detail to SLAC's Møller polarimeters by M. Swartz.¹³ The underlying ideas require a detail understanding of the atomic physics in the Fe atom and a detailed understanding of the experimental geometry. The polarized electrons in the Fe atom lie in the M shell of the four occupied shells, K, L, M, and N. Two electrons carry the Fe magnetization (out of a total of 26), corresponding to a target polarization of $\approx 8\%$. The high-energy beam electrons scatter from all 26 electrons, and the deeply bound electrons in the K and L shells have a "Fermi" motion which influence the scattering through the relativistic kinematics. Although the transverse momentum

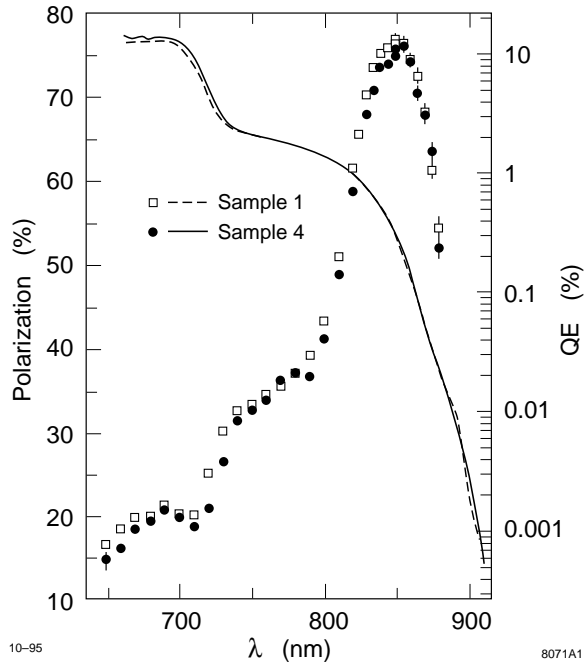


Figure 7: The polarization of the photoemitted electrons versus illuminating wavelength for two samples of strained gallium arsenide from a common wafer. The measurements were made in a Mott polarimeter at SLAC. The data points are the polarization (left-hand scale), and the solid and dashed curves are the quantum efficiencies (right-hand scale).

3.2 Møller Scattering

Møller scattering is a process well suited for high-energy electron beams. Polarimetry by this process utilizes the spin dependence of the cross section which at high energies is given by (neglecting masses)

$$\frac{d\sigma}{d\Omega} = \frac{\alpha^2}{s} \frac{(3 + \cos^2 \theta^*)}{\sin^4 \theta^*} \left[1 - \frac{\sin^2 \theta^*}{(3 + \cos^2 \theta^*)^2} P_b^z P_t^z (7 + \cos^2 \theta^*) \right],$$

where θ^* is the cms scattering angle, P_b^z is the longitudinal polarization component of the beam, P_t^z is the longitudinal component of spin of the target, and s is the cms energy squared. The angle in the lab for which $\theta^* = 90^\circ$ is $\theta_{lab} = \sqrt{2m_e/E_{beam}}$. This angle is 5.9 mrad for $E_{beam} = 29.13$ GeV. The

fering beam conditions. They are: (i) Mott scattering; (ii) Møller scattering; and (iii) Compton scattering. In these lectures the first and second will be described, since they contribute directly to the physics measurements being discussed here. The third technique, Compton scattering, is described elsewhere, but will not be discussed here since this technique was not used in the spin-structure program.

3.1 Mott Scattering

Mott scattering is the process in which electrons of low energy (20 KeV to several MeV) scatter in the Coulomb field of a high-Z nucleus. The technique generally used at SLAC is based on thin gold or uranium targets. The ability to measure electron beam polarization derives from the spin-orbit forces in the process, $\sigma = \sigma_0 + \sigma_1 \vec{L} \cdot \vec{S}$, where σ_0 and σ_1 are cross section terms dependent on energy, angle, and energy loss when the electron scatters.

For the incoming spin transverse to the beam direction,

$$\sigma(E_{\text{beam}}, \theta, \Delta E) = \sigma_0(E_{\text{beam}}, \theta, \Delta E)[1 + S(E_{\text{beam}}, \theta, \Delta E)P_e \sin \Phi],$$

where θ is the laboratory scattering angle, and Φ in the angle relative to the plane defined by the incoming electron direction and its transverse spin. Note that the spin of the electron must be oriented transverse to the incoming electron direction for this technique to work. Longitudinal components of the spin do not contribute significantly to Mott scattering. Originally, the function S (called the ‘‘Sherman function’’) was calculated from scattering theory. Today experimental values are used,¹⁰ giving an accuracy of approximately $\pm 2\%$. S has values from 0.1 to 0.4 for $\theta = 120^\circ$ in the lab and $E_{\text{beam}} = 120$ KeV to 1 MeV.

Measurement of scattering by two detectors placed at $\theta = 120$ degrees and $\Phi = \pm 90$ degrees is the usual arrangement to determine P_e . Cross sections are relatively large and statistical accuracy is generally very good. A typical measurement of two samples of strained GaAs at SLAC is shown in Figure 7, measured by a Mott system at SLAC.¹¹

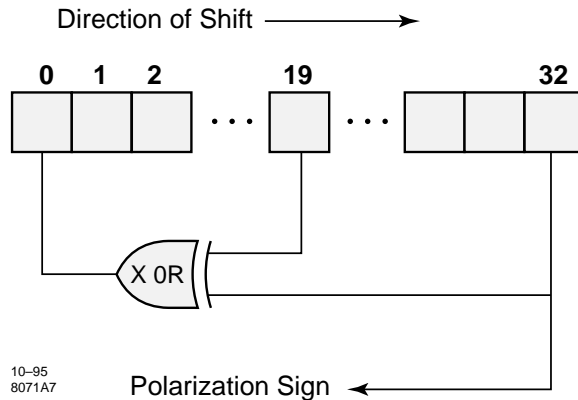


Figure 6: The electronic scheme for providing pseudorandom polarization sign bits. The algorithm indicated here develops a sequence of length $2^{33} - 1$ random bits which establishes the polarization sign for each machine pulse. The sequence is deterministic, so during data analysis offline, the sign bit can be validated for each pulse of the machine.

with feedback through an exclusive OR circuit, generates a polarization sign bit for each machine pulse. This pseudo-random generator has very useful properties which include: (i) the sequence of zeros and ones at the output is unbiased; (ii) the sequence doesn't repeat until $2^{33} - 1$ iterations, equivalent to over two years of running at 120 Hz; and (iii) any 33-bit sequence acts as a seed; given a sequence of 33 machine pulses with polarization sign bits, the entire future sequence is determined. This latter property allows the offline computer analyses to verify the integrity of the polarization sign bit. Failures in hardware show up offline as a failure of the recorded sequence to agree with the predicted sequence. During the course of the runs, the E143 experiment had a few infrequent glitches in the polarization sequence. These glitches were easily removed from the data stream without bias.

3 Polarimetry

Measurement of the magnitude of the electron polarization is of considerable importance to the experimental program. The errors contribute to the overall systematic errors and therefore must be kept small. At SLAC, three techniques for electron beam polarimetry have been used at various times and under dif-

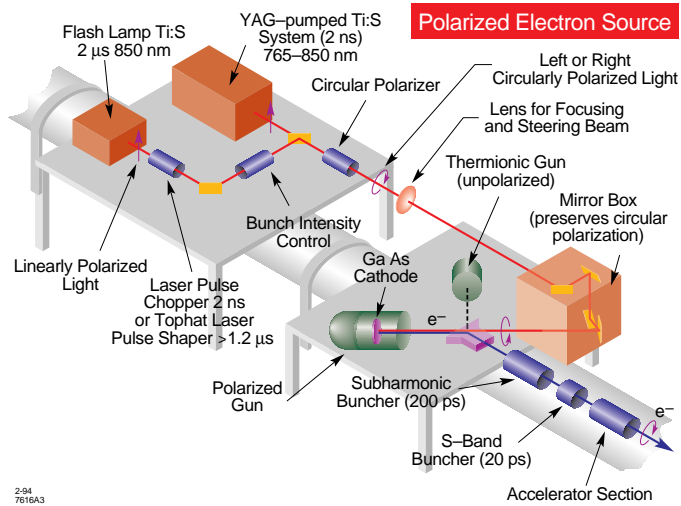


Figure 5: The layout of the lasers and the polarized electron gun at the accelerator injector is shown schematically. Two types of lasers are used, one for the SLC, which produces two 2 nsec pulses separated by 61 nsec, and one for the fixed target experiments, which produces a pulse 2 μ sec long.

tion, “short” pulses about 2 nsec are used.) The laser beams are transported, polarized, and focused onto the GaAs cathodes located in the gun structure. Photoemitted electrons leave the gun at 120 KeV kinetic energy, and are deflected onto the axis of the injector to the accelerator.

Performance results from three years of operating experience have been excellent. The important property for a source is the overall time of operation and the reliability achieved. The SLAC polarized electron source has been used for a total integrated time of 18,600 hours, and the availability has been $\geq 98\%$ during this period. The experiments using the photoemission source have enjoyed essentially trouble-free performance.

An important feature of the SLAC source is the ability to reverse polarization on a pulse-to-pulse basis. For asymmetries measured with the rapid reversal pattern, systematic effects that arise from drifts in detector efficiencies, target parameters, or beam monitors tend to be averaged out. Each beam pulse is assigned a polarization sign. The sequence of polarization signs which has been used for some time is illustrated in Figure 6.⁹ A shift register,

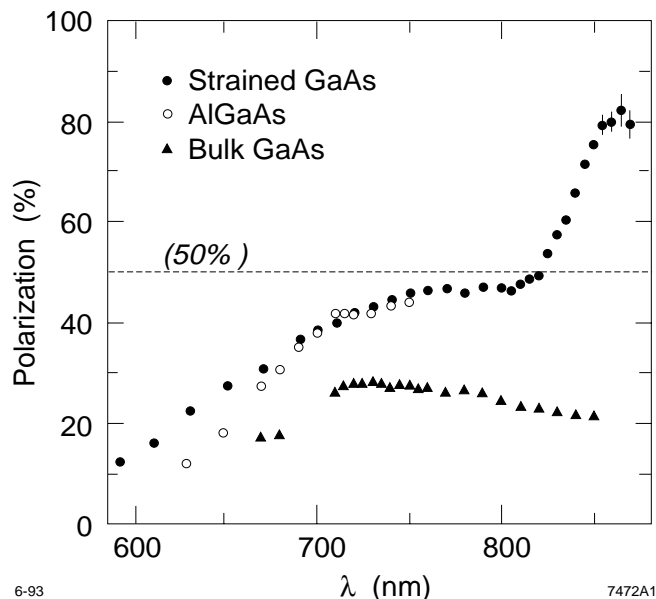


Figure 4: The polarization versus wavelength for three different cathodes that have run on the SLAC accelerator. The bulk GaAs cathode delivered beam to the SLC in 1992. The AlGaAs cathode was used for a fixed target experiment in 1992. The strained GaAs cathode has been used for both fixed target running and SLC since 1993.

for three types of materials used in SLAC experiments. The strained materials are seen to develop high polarization for $\lambda \approx 850$ nm.

SLAC has used several laser technologies in these photoemission sources. Earlier experiments using unstrained GaAs cathodes material operated at $\lambda = 720$ nm, and used a dye laser, common at the time. More recently titanium-sapphire lasers have been used, at $\lambda = 850$ nm. The quantum efficiency (QE) of the cathodes vary widely. At shorter wavelengths, $\lambda = 720$ nm, the QE achieved was as high as 10%. At the longer wavelengths, the QE values achieved has been from 0.1% to 1.0%. Laser energies used for the strained GaAs cathodes have been as high as 100 μ Joules per pulse at pulse rates of 120 Hz.

Figure 5 shows schematically the polarized electron source at the injector.⁵ For fixed target experiments, a flashlamp-pumped titanium-sapphire laser generates “long” pulses, about 2 μ sec at 120 Hz. (For the SLAC SLC configura-

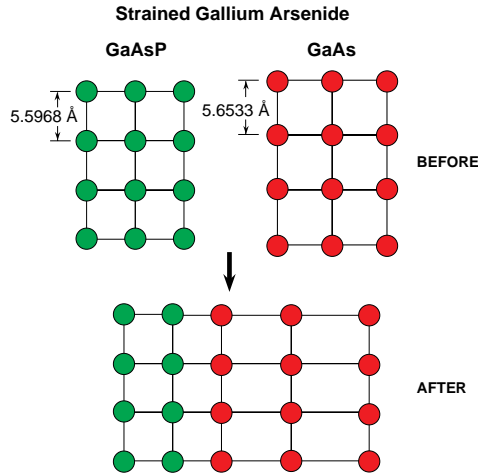


Figure 3: A thin layer of gallium arsenide crystal is distorted when deposited over a thicker layer of gallium arsenide phosphide of smaller lattice spacing.

ing to 600 degrees celsius for about 1 minute. After cooling, cesium is added to the surface in the presence of NF_3 , which provides fluorine for aiding the binding of the cesium. The exact procedures are described elsewhere⁵, but the process of activation of a GaAs cathode remains today somewhat of a black art.

Recent advances in the studies of GaAs have shown that internal strains from mechanical compression can lead to higher polarization.^{6,7} By distorting the crystalline structure, internal fields perturb the levels of the valence band differently for $m_z = \pm 1/2$ and $m_z = \pm 3/2$, as indicated in Figure 2. At the longest wavelengths for which electrons can be excited up to the conduction band, only $m_z = \pm 3/2$ levels contribute to photoexcitation, yielding $\pm 100\%$ polarization in the conduction-band electrons.

Mechanical strain is today rather straightforward to achieve. The processes known as MBE (for molecular beam epitaxy) and MOCVD (for metal organic chemical vapor deposition)⁸ both allow for deposition of thin layers of GaAs onto thicker layers of similar type material. To develop strain, GaAs is deposited onto a thick underlayer of $\text{GaAs}_x\text{P}_{1-x}$ (for $x \approx 0.28$) which itself has been grown on a substrate of GaAs. Figure 3 illustrates the distortions that develop in the thin layer. Figure 4 shows the polarization versus laser λ

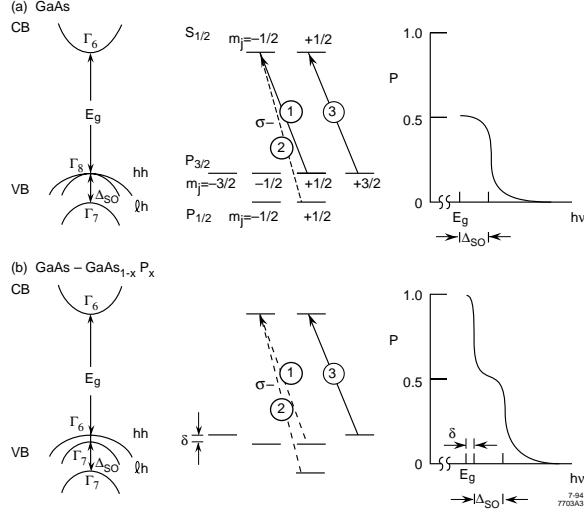


Figure 2: The energy level diagrams and transitions for σ^- excitation are shown schematically for (a) unstrained GaAs and (b) strained GaAs. Note that the degeneracy in the substates of the $P_{3/2}$ valence band for the unstrained GaAs (a) is broken in the strained GaAs (b) material. The electron polarization versus $h\nu$ for the excitation photon is also indicated.

the rapid, systematic-free reversals of polarization needed for the high-energy experiments.

Figure 2 shows a somewhat simplified energy level diagram for GaAs and its related III-V series compounds (such as AlGaAs, GaAsP, InAs, InGaAs, InP, etc.). Since GaAs is by now a widely used commercially available semiconductor material, considerable experimental and theoretical facts are known. Electrons in the valence band have $j=3/2$ symmetry in their wave functions, while the conduction band electrons have $j=1/2$ symmetry. Excitation of electrons from the unpolarized valence-band states to the conduction-band states by circularly polarized light populates the $m_z = -1/2$ level and the $m_z = +1/2$ level in the ratio 3:1. This simple picture predicts a $\pm 50\%$ polarization for the conduction band electrons.

To extract these conduction band electrons with reasonable efficiency, the surface of the GaAs must be clean and coated with cesium. Cleaning of the GaAs surface is accomplished in the gun structure in ultrahigh vacuum by heat-

by electric dipole transition, preserving the electron spin as it became free in the continuum. The stripped electrons were repelled toward the exit of the source by the electrostatic field in the region of the stripping process. Electrons would leave through the exit of the cathode region into the magnetic field of the holding coil which defined the longitudinal spin direction along the axis of the accelerator. These electrons were ejected from the region at 77 KeV kinetic energy, and were transported to the injector of the linear accelerator for acceleration to high energies. Reversal of the holding field reversed the longitudinal projection of the electron spin.

The operating parameters of the PEGGY source are well documented. Typical values were (i) peak currents of 0.2 milliamperes, (ii) pulse widths of the order of 2 μ sec; (iii) charge per linac pulse on the target $\leq 2.5 \times 10^9$ electrons; (iv) polarization ≈ 80 –90%; and (v) reversals of the beam polarization in several seconds. This source operated at SLAC from 1974 to 1981. Two experiments in spin structure of the proton, E80 and E130, ran during this period. An early search for parity violation, E95, also operated with this source.³

By 1974 the desire to look for electroweak effects in inelastic electron scattering led to a new proposal for a more intense polarized electron source. This proposal required a substantially higher intensity and the ability to reverse rapidly the polarization of the electron bunches without affecting the beam parameters. It was essential that the reversals of spin be accomplished free from influence on the intensity, beam position, beam direction, or beam phase space. High reliability and ease of operation of the polarized source were also important requirements.

Among the possibilities considered, photoemission from GaAs became the technique of choice.⁴ The GaAs source under consideration utilized a commercially available dye-laser technology. Rapid systematic-free reversals of the electron spin were to be accomplished with optical reversals of the laser circular polarization using a Pockels cell. The Pockels cell has the important property that high voltages (typically ± 2.5 KV) drive the optical cell into $\pm \lambda/4$ retardation which, coupled with incoming linear polarization from the laser, generates $\pm 100\%$ circular polarization in the laser beam. In the photoemission process from GaAs surfaces, the resulting photoemitted electrons have \pm longitudinal polarization. The use of the Pockels cell for spin reversals accomplished

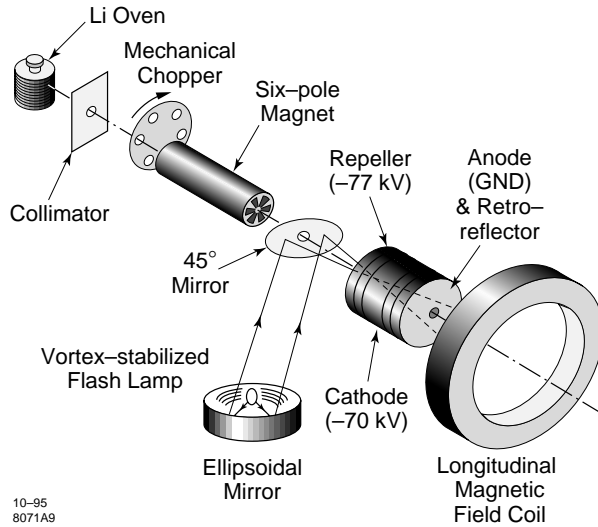


Figure 1: A schematic diagram of the original Yale-SLAC polarized electron source based on photoionization of a state-selected atomic beam of ${}^6\text{Li}$.

using first a photoionization source called “PEGGY,” and more recently a laser-driven GaAs photoemission source.

The photoemission source² was based on the separation of atomic beam spin states in a non-uniform magnetic field, first demonstrated in 1921 in the Stern-Gerlach experiments. Figure 1 shows schematically the PEGGY source, developed at Yale University and SLAC. An atomic beam of ${}^6\text{Li}$ is generated in an oven with a small orifice through which the hot atoms are emitted. The atomic beam passed through a collimator which cleaned up the off-axis atoms, and then through a mechanical chopper which removed the out-of-time atoms. This beam then passed into a sextupole magnet, for which the magnetic fields were zero on the axis but grew rapidly in magnitude off the central axis. One spin state (that is, for the spin projection aligned along the local field) of the ${}^6\text{Li}$ beam was focused, while the other spin state was defocused by this sextupole field. Successive collimators scraped away the unwanted spin state, but allowed the desired state to pass. A high-intensity argon flashlamp generated ultraviolet light which, when focused onto the atomic beam, stripped the valence electron from the atom. The stripping process proceeded largely

Table 1: Past, Present, and Future Experiments

Exp		Year	Nucleon	Target
E80	Yale-SLAC	1987	p	butanol
E130	Yale-SLAC	1983	p	butanol
EMC	CERN	1988	p	ammonia
SMC	CERN	1993	d	butanol
E142	SLAC	1993	n	helium-3 gas
SMC	CERN	1994	p	butanol
E143	SLAC	1994	p/d	ammonia
SMC	CERN	1995	d	butanol
E154	SLAC / 50 GeV	1995	n	helium-3 gas
HERMES	DESY HERA	1995	n	helium-3 gas
E155	SLAC / 50 GeV	1995	p/d	ammonia
HMC	CERN L-O-I	?	p/d	NH ₃ /butanol

2 Polarized Electrons

The spin of the electron has been an important part of fundamental particle physics since the advent of quantum mechanics and the understanding of the atomic spectra. Polarized electrons have been used as a tool to probe the physical properties of matter, for condensed matter studies, atomic physics, nuclear physics, and high-energy physics. Sources of polarized electrons have been sought with various properties, including the important objectives of improving the brightness and the degree of polarization. Control of the spin direction from the source has also been an important objective. The ease of the reversibility of the spin has been important to experimental use.

Examples of successful sources include: (i) β -decay of radioactive nuclei; (ii) low energy (Mott) scattering from nuclei; (iii) Photoionization of state-selected atomic beams; (iv) optical pumping of alkali atoms in vapor form; (v) ionization of polarized metastable ^4He ; (vi) storage ring beams; and (vii) photoemission from surfaces, including III-V semiconductors such as gallium arsenide (GaAs).

Linear accelerators require high-intensity and high-brightness sources. The pulsed structure of linacs require electron sources to be pulsed with a similar time structure. SLAC has operated with polarized electrons since 1974,

Outline

Lecture I:

1. A Brief History
2. Polarized Electrons
3. Polarimetry
4. The SLAC Spectrometers
5. Radiative Corrections

Lecture II:

6. The Proton Measurements
7. Neutron Targets
8. The Deuterium and ^3He Data
9. The g_2 Structure Function
10. The 50 GeV Upgrade

1 A Brief History

The history of nucleon spin-structure measurements goes back to the early days of inelastic electron scattering at SLAC, when Vernon Hughes came with a proposal to accelerate polarized electrons to high energy and to study inelastic scattering from a polarized proton target. The quark model of the proton was new at the time, and the spin-dependent structure functions were an excellent testing ground for that model. The proposal developed into an experiment which became SLAC experiment E80. Subsequent experiments followed those early studies, leading to E130 at SLAC, then EMC at CERN, and a host of later experiments. In 1988 the EMC Collaboration published the first data to reach low x . The asymmetries EMC observed fell below quark model expectations, and the experimentally measured proton sum rule indicated that the spin of the quarks contributed little to the proton spin. The subject of nucleon spin-dependent structure functions was stimulated by this surprising result from EMC, to become known as the “spin crisis.”¹ The continuation of the spin-structure studies at SLAC, which have been very active in recent years, was stimulated by the successful development of high-intensity beams of polarized electrons. Table I lists the past, present, and planned programs and experiments that grew out of the early work.

SLAC-PUB-7040
March 1996

An Overview of the SLAC Results*

Charles Y. Prescott

*Stanford Linear Accelerator Center
Stanford University, Stanford CA 94309*

e-mail: prescott@slac.stanford.edu

Invited talk presented at the Ettore Majorana

International School of Nucleon Structure: 1st Course:

The Spin Structure of the Nucleon, Erice, Italy, August 3-10, 1995

* Work supported by Department of Energy contract DE-AC03-76SF00515.